

# Unconventional multiferroicity induced by structural distortion and magnetostriction effect in the layered spin-1/2 ferrimagnet $\text{Bi}_2\text{Cu}_5\text{B}_4\text{O}_{14}$

Arkadeb Pal <sup>1</sup>, T. W. Yen,<sup>1,2</sup> T. W. Kuo,<sup>1</sup> C. W. Wang,<sup>3</sup> S. M. Huang,<sup>1</sup> M. C. Chou,<sup>2</sup> Y. C. Lai,<sup>3</sup> Y. C. Chuang <sup>3</sup>, P. Yanda,<sup>4</sup> A. Sundaresan <sup>4</sup>, H. S. Kunwar,<sup>5</sup> V. G. Sathe <sup>5</sup>, Ajay Tiwari <sup>1</sup>, D. Chandrasekhar Kakarla <sup>1</sup> and H. D. Yang <sup>1,2,\*</sup>

<sup>1</sup>Department of Physics, National Sun Yat-sen University, Kaohsiung 804, Taiwan

<sup>2</sup>Center of Crystal Research, National Sun Yat-sen University, Kaohsiung 804, Taiwan

<sup>3</sup>National Synchrotron Radiation Research Center, Hsinchu, 30076, Taiwan

<sup>4</sup>School of Advanced Materials, and Chemistry and Physics of Materials Unit, Jawaharlal Nehru Centre for Advanced Scientific Research, Jakkur, Bangalore-560064, India

<sup>5</sup>UGC-DAE Consortium for Scientific Research, University Campus, Khandwa Road, Indore-452001, India



(Received 4 January 2023; revised 3 April 2023; accepted 12 April 2023; published 15 May 2023)

Complex systems with strongly entangled microscopic degrees of freedom often host a plethora of exotic properties. Herein, we report the unconventional and interesting multiferroic behavior of a layered noncentrosymmetric ferrimagnetic spin-1/2 system,  $\text{Bi}_2\text{Cu}_5\text{B}_4\text{O}_{14}$ . Neutron powder-diffraction study deciphers a robust ferrimagnetic ( $\uparrow\downarrow\downarrow\downarrow$ ) ordering below a temperature  $T_C = 25$  K, which remains unaltered even under a high magnetic field of  $H = 10$  T. Interestingly, two successive ferroelectric transitions are observed, one of which is triggered by the magnetostriction effect and emerges concomitantly with the ferrimagnetic ordering at  $T_C = T_{E2} = 25$  K. This is accompanied by a pronounced dielectric peak and a prominent magnetodielectric coupling at  $T_C$ . By contrast, other ferroelectric transition commences in the paramagnetic state at  $T_{E1} = 32$  K, which is solely caused by a prominent structural distortion. This strong structural distortion is revealed by the synchrotron x-ray-diffraction study, which is further supported by a concurrent, sharp, anomalous phonon softening observed in the Raman spectra.

DOI: [10.1103/PhysRevB.107.184430](https://doi.org/10.1103/PhysRevB.107.184430)

## I. INTRODUCTION

Multiferroicity is an exotic phenomenon that exhibits two or more ferroic orders simultaneously in a single phase of a system, thus providing multiple controlling parameters [1–6]. Investigations into novel multiferroic materials have burgeoned over the past two decades owing to their intriguing rich physics and potential for harnessing novel spintronic devices. Nevertheless, unraveling a new multiferroic material is difficult because the magnetic and ferroelectric orders are constrained by mutually antagonistic and stringent symmetry requirements [1,4]. Generally, multiferroic properties are observed in antiferromagnetic systems; however, ferromagnetic or ferrimagnetic multiferroic materials are more interesting and advantageous, as they demonstrate net spontaneous magnetization. However, to satisfy the increasing demand for futuristic spintronic devices, more effort is required to discover new multiferroic materials with enhanced functionalities [7]. Apart from their far-reaching application prospects, the discovery and study of new multiferroics allows one to better understand some of the enduring challenges associated with condensed-matter physics, which are in fact related to the coupled behavior of spin, orbital, lattice, and phonon degrees in a system [1,4,8–11]. Moreover, the magnetodielectric effect is an intriguing phenomenon that can facilitate the

understanding regarding the mutual relationship between spin and dipolar properties [10,12–14]. Recent studies have shown that unique properties such as multipole order and magnetic quantum criticality can be effectively gauged by investigating the magnetodielectric effect [14,15].

In this context, the oxocuprate compound,  $\text{Bi}_2\text{Cu}_5\text{B}_4\text{O}_{14}$  (BCBO), is of particular interest. In 2002, Petrakovskii *et al.* first reported the growth and initial structural and magnetic properties of BCBO, wherein a centrosymmetric structure with  $P\bar{1}$  symmetry was proposed [16]. Meanwhile, in 2008, Pan *et al.* proved that BCBO exhibits a noncentrosymmetric (NCS) polar crystal structure with  $P1$  symmetry by performing both a second-harmonic generation study and an extensive structural analysis [17]. Furthermore, they determined the Wyckoff positions of the atoms, which were used in the present study. Subsequently, Arjun *et al.* investigated its magnetic properties by studying its bulk magnetization and specific-heat properties [18]. Spin-1/2 magnets often host exotic phenomena such as superconductivity, spin liquid state, and multiferroicity [19–21]. In particular, a number of spin-1/2  $\text{Cu}^{2+}$  compounds exhibited fascinating multiferroic properties, including high critical temperature (high- $T_C$ ) multiferroic  $\text{CuO}$  ( $T_C \sim 230$  K),  $\text{Cu}_2\text{OCl}_2$  ( $T_C \sim 70$  K), and skyrmion-hosting multiferroic  $\text{Cu}_2\text{OSeO}_3$  [21–23]. Furthermore, a number of magnetic systems with polar NCS crystal structure in their paramagnetic state, such as  $M_2\text{Mo}_3\text{O}_8$  ( $M = \text{Co}, \text{Mn}, \text{Fe}$ ),  $\text{Ni}_3\text{TeO}_6$ , and  $R\text{FeWO}_6$  ( $R = \text{Tb}, \text{Y}, \text{Eu}, \text{Dy}, \text{Ho}$ ), have received significant research interests in the

\*yang@mail.nsysu.edu.tw

recent years due to the exhibition of multiferroic properties in their ordered magnetic states [24–29]. In fact, such polar magnets form a new class of multiferroics, which is distinct from the well-known type-II multiferroicity, wherein the inversion symmetry is broken only below the magnetic ordering [29]. Thus, the polar NCS structure of BCBO may be a potential source for hosting the multiferroicity in this system [28]. Moreover, the unconventional layered structure of BCBO formed by pentamer Cu units [which is distinct from the typical two-dimensional (2D) lattice] makes it a unique spin-lattice system, which may result in nontrivial exotic phenomena. The facts above motivated us to comprehensively investigate the multiferroic property of BCBO.

## II. EXPERIMENTAL AND COMPUTATIONAL METHODS

A polycrystalline sample of BCBO was prepared using a standard solid-state reaction method, which is described in the Supplemental Material (SM) [30]. Synchrotron x-ray-diffraction (SXR) measurements were performed at the 19A beamline (with radiation of  $\lambda = 0.77489 \text{ \AA}$  and  $0.619920 \text{ \AA}$  for room-temperature and low-temperature SXR measurements, respectively) of the Taiwan Photon Source at the National Synchrotron Radiation Research Center. A commercial superconducting quantum interference device-based magnetometer (Quantum Design) was employed for magnetization- and magnetic-field-dependent electrical measurements. Neutron powder-diffraction (NPD) measurements were carried out on the high-intensity neutron powder diffractometer (with  $\lambda = 2.41 \text{ \AA}$  neutrons), WOMBAT [31], at the Australian Nuclear Science and Technology Organization, Sydney. Raman spectroscopy was performed using a HORIBA Jobin Yvon HR-800 spectrometer. The Vienna *Ab initio* Simulation Package (version 6.1.2) was used to perform theoretical calculations of the BCBO. More related information is provided in the SM [30].

## III. RESULTS AND DISCUSSION

### A. Crystal structure

The high-resolution SXR pattern at  $T = 300 \text{ K}$ , along with its Rietveld refinement, is shown in Fig. S1 of the SM [30]. The refinement yielded a polar NCS triclinic structure with  $P1$  symmetry, thus agreeing with the previous study [18]. Upon lowering the temperature down to  $T = 14 \text{ K}$ , no global structural phase transition was observed, which is evident from Figs. 1(a) and 1(b) demonstrating the refined SXR patterns at  $T = 100$  and  $14 \text{ K}$ , respectively. The various refined crystallographic parameters (such as lattice parameters and Wyckoff positions) at  $T = 100 \text{ K}$  are summarized in Table SI of the SM, which are consistent with previously reported values [18]. The crystal structure of BCBO (as viewed on the  $ab$  plane), which is based on zigzag sheets of planar rectangular  $\text{CuO}_4$  plaquettes and trigonal pyroborate  $\text{BO}_3$  groups, is schematically demonstrated in Fig. 1(c).

### B. Magnetization properties

The thermal variation of the magnetization ( $M$ ) curves under an applied magnetic field ( $H$ ) of  $0.1 \text{ T}$  based on

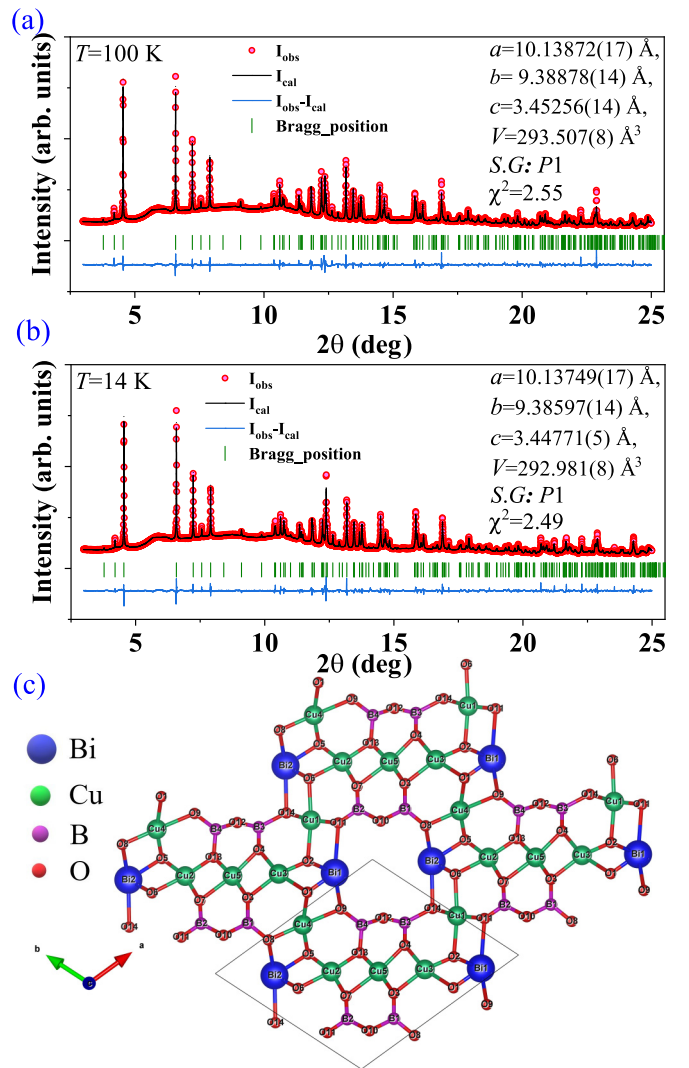


FIG. 1. (a) and (b), respectively, depict SXR patterns at  $T = 100$  and  $14 \text{ K}$  along with their Rietveld refinements. Red circles represent the data, while the black solid line is the calculated Rietveld refined profile. Green vertical bars refer to the Bragg positions. Herein, the radiation had a wavelength of  $\lambda = 0.619920 \text{ \AA}$ . (c) Pictorial representation of BCBO atomic structure viewed on  $ab$  plane as derived from the SXR pattern (at  $T = 90 \text{ K}$ ) analysis. The structure is made up of zigzag sheets of planar rectangular  $\text{CuO}_4$  plaquettes and trigonal pyroborate  $\text{BO}_3$  groups. Here, the linear  $\text{Cu}_3\text{O}_8$  trimers formed by the edge-shared coplanar  $\text{CuO}_4$  [involving  $\text{Cu}(2)$ ,  $\text{Cu}(5)$ , and  $\text{Cu}(3)$ ] units are bordered by two Bi atoms at their sides. Each  $\text{Cu}_3\text{O}_8$  trimer is further joined with two noncoplanar  $\text{CuO}_4$  units [containing  $\text{Cu}(4)$  and  $\text{Cu}(1)$ ] by corner sharing, thus leading to a pentamer unit. The presence of the corner-shared pyroborate  $\text{BO}_3$  groups provides weaker exchange interaction pathways between  $\text{Cu}^{2+}$  ions [i.e.,  $\text{Cu}(5)$  gets connected to  $\text{Cu}(1)$  and  $\text{Cu}(4)$ ] in the pentamer units, which essentially leads to a frustrated triangular network. These layered networks of pentamer Cu units are separated along the  $c$  axis.

conventional zero-field cooling (ZFC) and field-cooling (FC) protocols are demonstrated in Fig. 2(a). A sharp increase in the magnetization is observed at  $T_C \sim 25 \text{ K}$ , which essentially signals a long-range ordered (LRO)

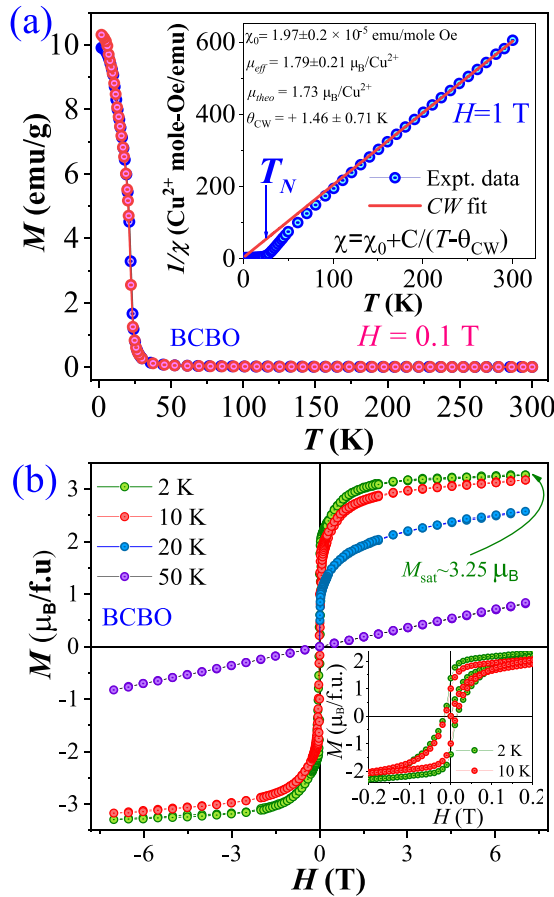


FIG. 2. (a)  $T$ -dependent magnetization curves following ZFC and FC under a magnetic field of  $H = 0.1$  T. The inset demonstrates the Curie-Weiss fit of “ $1/\chi$  vs  $T$ ” curve at  $H = 1$  T. (b) shows  $M(H)$  curves collected at 2, 10, 20, and 50 K. Inset: A close view of the  $M(H)$  curves collected at  $T = 2$  and 10 K in the low- $H$  range. Observed hysteresis is typical of an FiM system. For all these curves, the associated error bars are smaller than the data point markers.

ferromagnetic (FM) or ferrimagnetic (FiM) state. This finding is consistent with that of an earlier report [18]. Moreover, the “inverse susceptibility ( $1/\chi$ ) vs  $T$ ” data under  $H = 1$  T was fitted in the sufficiently elevated temperature range ( $T > 150$  K) using the standard Curie-Weiss (CW) law:  $\chi = \chi_0 + \frac{C}{T - \theta_{CW}}$ , where  $\chi_0$  combines two different terms, i.e., the core diamagnetism emanating from the core-electron shells ( $\chi_{core}$ ) of the  $\text{Cu}^{2+}$  ions of BCBO and its open-shell’s Van Vleck paramagnetism ( $\chi_{VV}$ ); the Curie constant is represented by  $C$ , and the characteristic CW temperature is denoted by  $\theta_{CW}$ . The best fit is shown in the inset of Fig. 2(a). The best fitting yielded  $\chi_0 = 1.97 \pm 0.2 \times 10^{-5}$  emu/(mole-Oe),  $\mu_{\text{eff}} = 1.79 \pm 0.21 \mu_B/\text{Cu}^{2+}$ , and  $\theta_{CW} = +1.46 \pm 0.71$  K. The positive sign of  $\theta_{CW}$  indicates dominant FM interactions in BCBO. Furthermore, the observed  $\mu_{\text{eff}} = 1.79 \mu_B/\text{Cu}^{2+}$  closely matches the spin-only moment of  $\text{Cu}^{2+}$  ions, i.e.,  $\mu_{\text{theo}} = 1.73 \mu_B/\text{Cu}^{2+}$ .

Figure 2(b) shows the isothermal  $H$  variation of magnetization, i.e.,  $M(H)$  curves recorded at  $T = 2, 10, 20,$  and  $50$  K. The  $M(H)$  curves collected below  $T_C$  demonstrate the typical features of the FM or FiM state, although the  $M(H)$  curves

indicate magnetization saturation below  $T_C$ , but it still show a nonzero slope (i.e.,  $dM/dH$ ) even at a high field of  $H = 7$  T, which can be presumably attributed to the small and gradual field-forced spin realignment with increasing  $H$ . The highest value of saturation magnetization ( $M_{\text{sat}}$ ) at  $T = 2$  K and  $H = 7$  T is  $\sim 3.25 \mu_B/\text{f.u.}$ , which is lower than the value of  $M_{\text{sat}} = 5 \mu_B/\text{f.u.}$ , as is expected for an FM spin structure. Hence, this suggests an FiM spin structure with a possible  $\uparrow\downarrow\downarrow\downarrow$   $\text{Cu}$ -spin structure (resulting in an expected  $M_{\text{sat}} \sim 3 \mu_B/\text{f.u.}$ ), which is also suggested by our NPD analysis (which will be discussed later). The  $M(H)$  curve at  $T = 50$  K shows a nonsaturating linear nature, thus suggesting a paramagnetic state, which is expected above  $T_C$ .

### C. Spin structure using neutron powder diffraction

To analyze the microscopic spin structure of BCBO, NPD measurements were carried out at various temperatures above and below  $T_C$ . Figures 3(a) and 3(b) show the NPD patterns along with their calculated Rietveld profiles for  $T = 250$  and  $29$  K, respectively, which are satisfactorily fitted (with value of  $\chi^2 = 6.29$  and  $6.77$  for  $T = 250$  and  $29$  K, respectively) solely with the nuclear structure having triclinic symmetry  $P1$ . The NPD patterns (raw) collected at three different temperatures  $T = 3.3, 26,$  and  $250$  K are shown in Fig. S2 of the SM [30]. Upon lowering the temperature below  $T_C$ , a set of Bragg reflections, such as  $(1\ 0\ 0)$ ,  $(1\ 1\ 0)$ ,  $(2\ -1\ 0)$ , and  $(1\ 2\ 0)$ , showed increase in their intensities, thus signaling the onset of the LRO state in BCBO. The thermal evolution of the intensity difference of NPD patterns relative to the NPD data at  $T = 29$  K, i.e., “ $I(T) - I(29\ \text{K})$ ” with varying  $T$  and  $2\theta$ , is shown via a color-coded contour plot in Fig. 3(d). This clearly indicates the emergence of magnetic Bragg peaks below  $T_C$ , thus confirming the occurrence of magnetic ordering below  $25$  K, which corroborates the magnetization results. Furthermore, to identify the spin structure of BCBO, the nuclear contribution was subtracted (using the reference of the NPD data at  $T = 29$  K) from the NPD data at  $T = 3.3$  K, which is shown in the lower panel (i) of Fig. 3(e). Thereafter, a spin structure analysis was performed for 32 different possible spin structures with various spin orientations. During NPD data analysis, the spatial symmetry  $P1$  was unchanged for both the crystalline and magnetic structures. To avoid complexity, the simulated NPD patterns only for the FM  $\downarrow\downarrow\downarrow\downarrow$  and FiM  $\uparrow\downarrow\downarrow\downarrow$  spin structures are shown in panels (ii) and (iii) of Fig. 3(e), respectively. The large dissimilarity between the experimentally observed NPD data and the simulated pattern for the FM  $\downarrow\downarrow\downarrow\downarrow$  spin structure preclude the FM state in BCBO. By contrast, the observed NPD pattern showed a close match with the simulated pattern for the FiM  $\uparrow\downarrow\downarrow\downarrow$  spin structure. In addition, a comparison of the observed NPD pattern with other simulated magnetic Bragg peaks for some other possible FiM spin structures, such as  $\downarrow\uparrow\downarrow\downarrow$ ,  $\downarrow\downarrow\uparrow\downarrow$ ,  $\downarrow\downarrow\downarrow\uparrow$ , and  $\downarrow\downarrow\downarrow\uparrow$ , has also been made in Fig. S3(a) of the SM [30]. This further suggests that FiM  $\uparrow\downarrow\downarrow\downarrow$  spin structure best describes the magnetic structure of BCBO. Moreover, the analysis suggests that all the Cu spins are aligned along the crystallographic  $c$  axis, whereas attempts to fit the data with spins in other directions failed, as evident from Fig. S3(b) of the SM [30]. Hence, our analysis

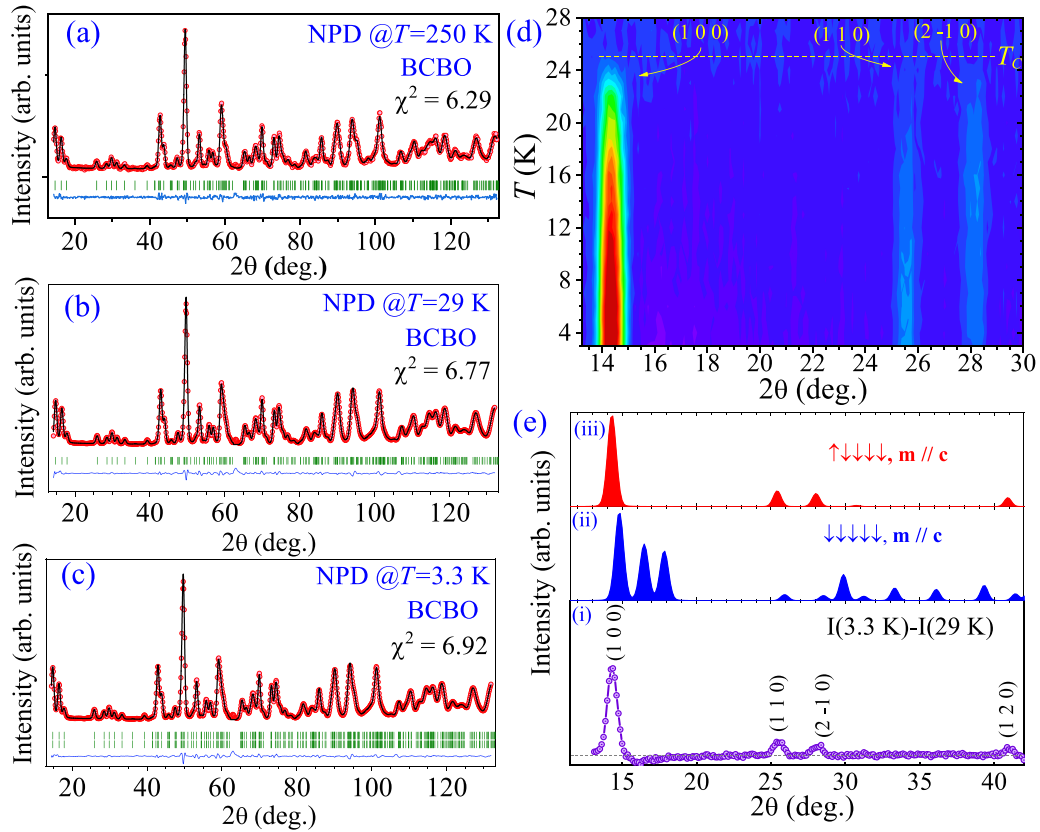


FIG. 3. (a), (b), and (c) demonstrate the NPD patterns of BCBO along with their Rietveld refinements at  $T = 250$ ,  $29$ , and  $3.3$  K respectively. (d) Color-coded contour plot of intensity difference of the neutron diffraction patterns with respect to the NPD data at  $T = 29$  K, i.e.,  $I(T) - I(29 \text{ K})$  as a function of  $T$  and  $2\theta$ . The plot clearly suggests an onset of a long-range magnetic ordering below  $T_C = 25$  K for a set of Bragg reflections, such as  $(1\ 0\ 0)$ ,  $(1\ 1\ 0)$ , and  $(2\ -1\ 0)$ , thus signaling a magnetic contribution. (e) Comparison of (i) experimentally observed magnetic Bragg peaks, i.e.,  $I(3.3 \text{ K}) - I(29 \text{ K})$  with simulated NPD patterns for (ii) FM ( $\downarrow\downarrow\downarrow\downarrow$ ) and (iii) FiM ( $\uparrow\downarrow\downarrow\downarrow$ ) order in BCBO. The observed pattern closely matches with FiM pattern, thus indicating an FiM ordering in BCBO. For all the NPD measurements, the wavelength of the neutrons was  $\lambda = 2.41 \text{ \AA}$ .

yields a commensurate FiM  $\uparrow\downarrow\downarrow\downarrow$  spin structure with a magnetic propagation vector  $k = (0, 0, 0)$ . The resulting refined NPD data at  $T = 3.3$  K based on a combination of nuclear ( $P1$ ) and magnetic ( $\uparrow\downarrow\downarrow\downarrow$ ) structures are shown in Fig. 3(c). An average moment of  $0.86 \pm 0.02 \mu_B/\text{Cu}$  was estimated from the analysis. The spin structure was composed of an FM linear  $\text{Cu}_3\text{O}_8$  trimer [i.e.,  $\text{Cu}(2)$ ,  $\text{Cu}(5)$ , and  $\text{Cu}(3)$  are parallel to each other], which is parallel to  $\text{Cu}(4)$ , unlike the only spin  $\text{Cu}(1)$  directed antiparallel to the FM trimer. A schematic representation of the aforementioned collinear FiM  $\uparrow\downarrow\downarrow\downarrow$  spin structure of BCBO is shown in Fig. 4(a). The obtained spin structure is consistent with the magnetization results, as it suggests a saturation moment of  $M_{\text{sat}} \approx 3 \mu_B/\text{f.u.}$  Moreover, for a magnetic phase transition from the PM to LRO state at  $T = T_C$ , the magnetic peak intensity can be expressed as  $I(T) = I_{\text{PM}} + [I_0(1 - T/T_C)^{2\beta}]$ , where the first and second terms refer to the intensity variations in the PM ( $> T_C$ ) and LRO regions ( $< T_C$ ), respectively.  $I_0$  is the intensity at  $T \rightarrow 0$  K, and  $\beta$  denotes the critical exponent that determines the nature of the magnetic ordering. The corresponding best fit to the “thermal variation of the integrated intensity of the magnetic reflection  $(1\ 0\ 0)$ ” is demonstrated in Fig. 4(b). The best fit yielded a transition temperature of  $T_C = 25.02(6)$  K and  $\beta = 0.295(7)$ . The unusual type of

layered spin-1/2 Cu spin lattice of BCBO may have resulted in a slightly lower value of  $\beta = 0.295(7)$  than the value expected for a three-dimensional (3D) Ising spin system ( $\beta = 0.325$ ). Nevertheless, it was much higher than the value expected for a 2D Ising spin system ( $\beta = 0.125$ ) and much smaller than the value desired for a 3D Heisenberg spin system ( $\beta = 0.367$ ) [32].

In addition, we performed NPD measurements under a high magnetic field of  $H = 10$  T to investigate whether BCBO exhibits any field-induced transition from the FiM ( $\uparrow\downarrow\downarrow\downarrow$ ) state to an FM ( $\downarrow\downarrow\downarrow\downarrow$ ) state. However, the results of an NPD pattern analysis based on  $T = 1.9$  K and  $H = 10$  T show that no such field-induced transitions occurred at such a high field [see Fig. 4(c)]. Hence, a robust FiM ( $\uparrow\downarrow\downarrow\downarrow$ ) spin structure exists in BCBO.

Furthermore, we performed density-functional theory (DFT)-based *ab initio* theoretical calculations to estimate the total energies of the present system with a spin structure similar to the experimentally observed FiM ( $\uparrow\downarrow\downarrow\downarrow$ ) state as well as an FM ( $\downarrow\downarrow\downarrow\downarrow$ ) state. Our calculations yielded a lower energy ( $E$ ) for the FiM state ( $E = -149.519$  eV/f.u.) as compared to that for the FM state ( $E = -149.472$  eV/f.u.), thus suggesting an energetically favorable FiM ground state for this system. This is in good agreement with the NPD results.

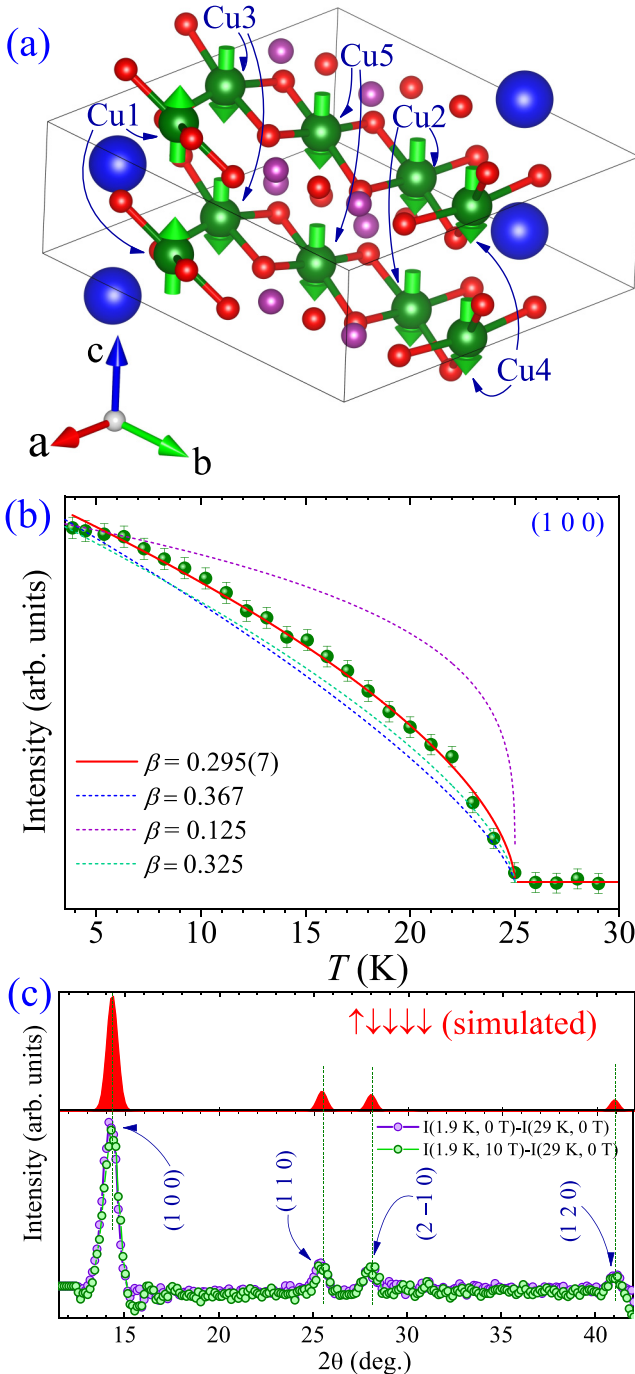


FIG. 4. (a) Pictorial representation of microscopic spin structure of BCBO, as determined from the NPD data (at  $T = 3.3$  K) analysis. An FiM ( $\uparrow\downarrow\downarrow\downarrow$ ) spin structure is obtained, wherein the spin Cu(1) is antiparallel to the FM sublattice formed by other four Cu spins, i.e., Cu(2) to Cu(5) spins. (b) Temperature evolution of intensity of magnetic Bragg reflection (1 0 0) and its critical exponent fitting. Red solid line refers to the best fitting with  $\beta = 0.295(7)$ , whereas the other dotted lines indicate the power-law behavior expected for various models, such as 3D Ising ( $\beta = 0.325$ ), 3D Heisenberg ( $\beta = 0.367$ ), and 2D Ising ( $\beta = 0.125$ ). (c) Upper panel: Simulated NPD pattern containing magnetic peaks for an FiM ( $\uparrow\downarrow\downarrow\downarrow$ ) spin structure with spins along  $c$  axis. This matches well with the experimentally observed NPD patterns (lower panel) collected under  $H = 0$  and 10 T. Lower panel: Comparison of the magnetic Bragg peaks in NPD patterns collected under

Details regarding the calculations and the corresponding electronic density of states are provided in the SM (Fig. S4).

#### D. Exhibition of magnetodielectric effect and ferroelectricity

The polar NCS structure and FiM spin ordering of BCBO render it an interesting system for dielectric and multiferroic property studies. The real part of the dielectric constant ( $\epsilon'$ ) of BCBO at various frequencies ( $f$ ) under  $H = 0$  T is shown in Fig. 5(a). Interestingly, two pronounced dielectric peaks emerged successively in the  $\epsilon'(T)$  curves in different temperature regions. The higher-temperature dielectric peaks demonstrated clear frequency dependence in the temperature range  $T = 78$ – $100$  K. The observed frequency dispersion is indicative of dielectric relaxation, which can be described using the typical Arrhenius relation  $\tau = \tau_0 \exp(\frac{E_a}{k_B T_M})$ , where  $E_a$  is the activation energy,  $\tau_0$  the characteristic relaxation time, and  $T_M$  the position of the dielectric local maximum at  $\tau = 1/2\pi f$ . The best fit, as shown in the inset (top) of Fig. 5(a), yielded  $E_a = 0.095 \pm 0.001$  eV and  $\tau_0 = 2.3 \pm 0.3 \times 10^{-12}$  s, which are within the range of values for other highly insulating oxide materials exhibiting relaxation behavior caused by local structural distortion [33]. Such structural distortion-driven dielectric relaxation has been observed previously in other magnetic insulators [34]. By contrast, the lower-temperature dielectric peaks exhibited  $f$ -independent nature and were positioned at the onset of FiM ordering temperature, i.e.,  $T_C \sim 25$  K, as shown in the inset (bottom) of Figs. 5(a) and 5(b). Moreover, the observed dielectric loss ( $\tan \delta$ ) in the entire  $T$  range of our study was insignificantly small ( $\sim 0.001$ ), which clearly indicates the highly insulating nature of BCBO, thus precluding any contribution from spurious experimental effects or extrinsic charge carriers to the  $\epsilon'(T)$  curves [10,28]. It should be noted here that a structural phase transition can also give rise to an  $f$ -independent dielectric anomaly. However, for the present case, a symmetry-lowering phase transition is not possible, as it belongs to  $P1$  symmetry (no. 001). Therefore, the observed  $f$ -independent dielectric peaks at  $T_C \sim 25$  K essentially signal an underlying inherent magnetodielectric effect [10,24]. We further investigated the  $\epsilon'(T)$  curves recorded at  $f = 100$  kHz under different applied  $H$  to validate the magnetodielectric coupling [Fig. 5(c)]. Interestingly, the lower-temperature dielectric peak at  $T_C$  exhibited a substantial decrease in  $\epsilon'$  as  $H$  is increased, as shown in the inset of Fig. 5(c). Conversely, the higher-temperature  $\epsilon'(T)$  peak remained almost unaffected by the applied  $H$ . As the maximum change in the  $\epsilon'(T)$  curves under an applied  $H$  was observed immediately below  $T_C$  [inset of Fig. 5(c)], we further recorded an “isothermal  $H$  variation of  $\epsilon'$ ” curve at  $T = 20$  K, as shown in Fig. 5(d).

$H = 0$  T (shown in violet color), i.e.,  $I(T = 1.9 \text{ K}, H = 0 \text{ T}) - I(T = 29 \text{ K}, H = 0 \text{ T})$  and under  $H = 10$  T (shown in green color) i.e.,  $I(T = 1.9 \text{ K}, H = 10 \text{ T}) - I(T = 29 \text{ K}, H = 0 \text{ T})$ . The application of the high magnetic field of  $H = 10$  T caused no noticeable change in the magnetic structure, which is evidenced from its NPD pattern displaying similar peaks as that of NPD pattern recorded under  $H = 0$  T. Here, the wavelength of the neutrons used was  $\lambda = 2.41$  Å.

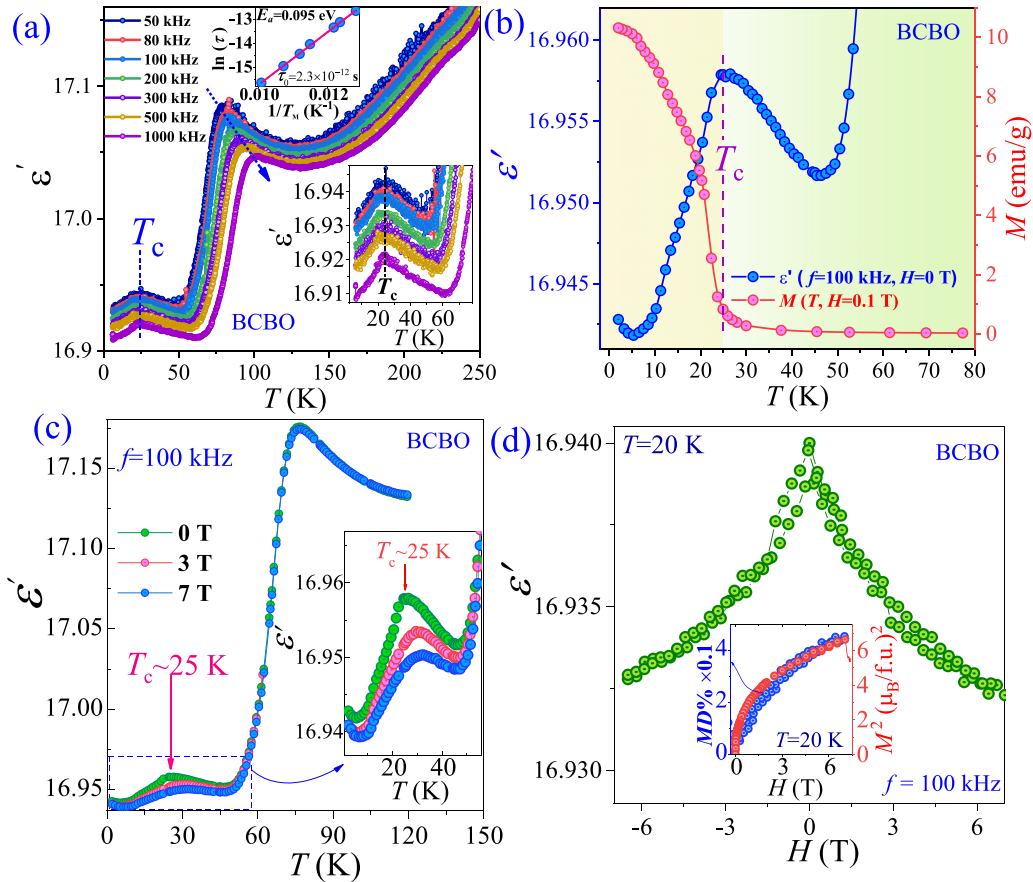


FIG. 5. (a)  $\varepsilon''(T)$  curves at different frequencies as indicated. Inset: Closer view of  $\varepsilon''(T)$  curves near  $T_c$ . (b) Compares the curves showing  $T$  variations of FC magnetization curve under  $H = 0.1$  T and dielectric constant ( $\varepsilon'$ ) at  $f = 100$  kHz. (c)  $\varepsilon''(T)$  curves collected under different magnetic fields. Inset: Enlarged view of  $\varepsilon''(T)$  curves near  $T_c$ . (d) Isothermal  $\varepsilon'$  variation as a function of  $H$  curve at  $T = 20$  K. Inset:  $MD\%$  (blue) and  $M^2$  (red) variations with respect to  $H$  at 20 K, thus demonstrating  $MD \propto M^2$  scaling behavior. For all these curves, the associated error bars are smaller than the data point markers.

As  $H$  was increased,  $\varepsilon'$  decreased monotonically, which suggests a profound magnetodielectric effect and thus marking a direct coupling between the spin and dipolar order parameters. Furthermore, the  $\varepsilon'(H)$  and  $M(H)$  curves recorded at  $T = 20$  K reasonably followed a scaling behavior that can be expressed as  $MD = \Delta\varepsilon' = [\varepsilon'(0) - \varepsilon'(H)]/\varepsilon'(0) \propto M^2$ , as shown in the inset of Fig. 5(d); in fact, this behavior is typically observed in systems demonstrating higher-order magnetoelectric coupling caused by the magnetostriction effect [10,35]. Moreover, pyrocurrent ( $I_p$ ) measurements were performed to probe the ferroelectric polarization ( $P$ ) of the system. Prior to measuring the  $I_p(T)$  curves, the sample was cooled under two opposite-poling electric fields,  $E_p = \pm 7.5$  kV/cm; subsequently, the sample was shorted for 30 min at  $T = 2$  K, and the  $I_p(T)$  curves were recorded during heating. Interestingly, two different  $I_p$  peaks were observed, which were successively positioned at  $T_{E1} \sim 32$  K and  $T_{E2} \sim 25$  K [Fig. 6(a)]. This indicates the onset of two successive ferroelectric transitions in BCBO. The  $I_p(T)$  and corresponding  $P(T)$  curves [Fig. 6(b)] demonstrate symmetrically opposite characteristics under opposite poling, thus confirming the reversibility of  $P$ . Below  $T = 20$  K, the saturated value of  $P$  was around  $18 \mu\text{C}/\text{m}^2$ . Additionally, the  $I_p(T)$  curves were recorded under three different warming rates and showed no

distinct shifts in their peak positions ( $T_E$ ), as shown in the inset of Fig. 6(c). These features are typically observed in systems showing a ferroelectric order [24,36]. Moreover, to further validate the presence of two successive ferroelectric transitions, we carried out pyrocurrent ( $I_p$ ) measurements with different poling temperatures ( $T_p$ ) above and below  $T_{E1} \sim 32$  K and  $T_C = T_{E2} \sim 25$  K. During this process, a poling field of  $E_{\text{pol}} = 9$  kV/cm was applied at different  $T_p$  and subsequently, the sample was cooled to the lowest temperature ( $T = 2$  K) [37,38]. The various  $I_p(T)$  curves so obtained are described in Fig. 6(d). It is observed that the  $I_p$  peak at  $T_C = T_{E2}$  is less conspicuous as compared to that at  $T_{E1}$ , for the  $T_p$  lying above  $T_{E1}$  or slightly above  $T_{E2}$ . On the contrary, the  $I_p$  peak at  $T_C = T_{E2}$  progressively becomes more pronounced and starts dominating over the peak at  $T_{E1}$ , as  $T_p$  approaches close to  $T_C = T_{E2}$  or goes beyond it. Nevertheless, for all the cases, both the  $I_p$  peaks at  $T_{E1}$  and  $T_{E2}$  were present, which further attests to the presence of two ferroelectric transitions in this polar magnet BCBO, wherein changes in  $P$  takes place. A similar behavior of the  $I_p(T)$  curves was also reported previously in other multiferroics exhibiting double-ferroelectric transitions [37]. As a matter of fact, although the  $I_p(T)$  curves exhibit two successive peaks, the dielectric study only reveals a single broad peak near  $T_C = T_{E2}$ . It may be possible that the

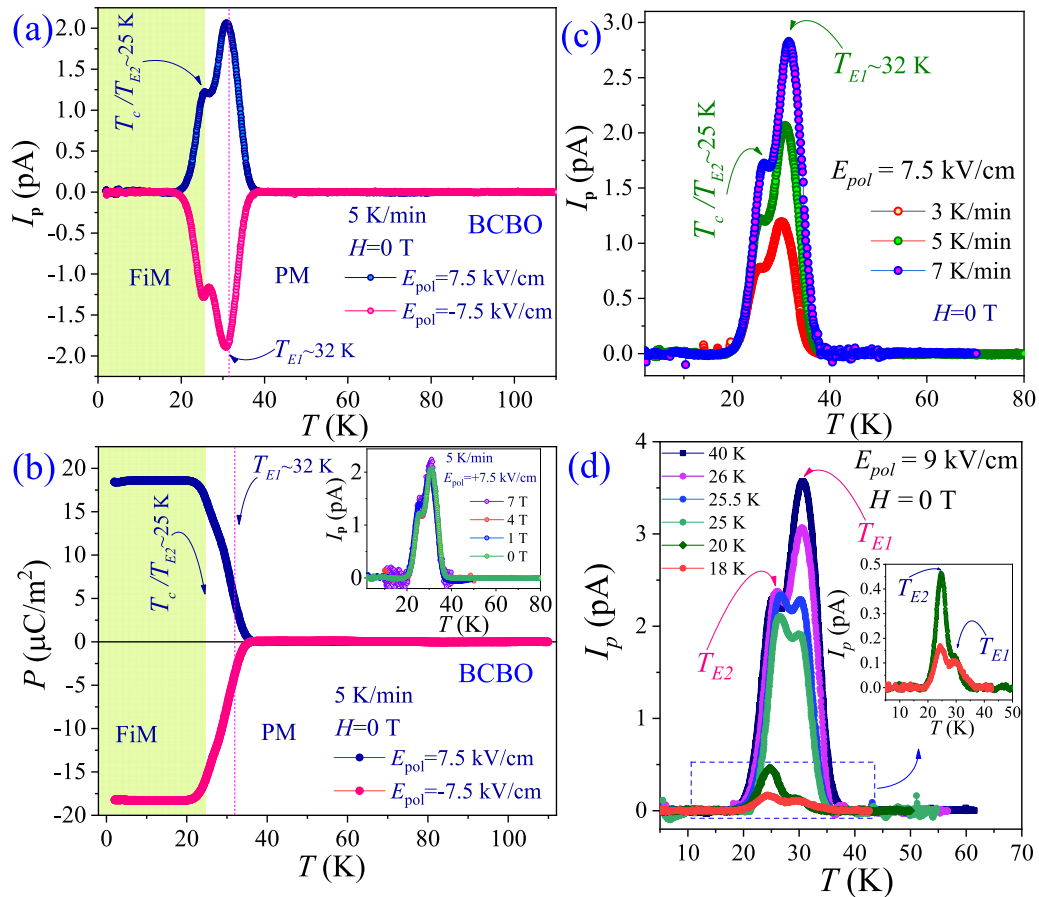


FIG. 6. (a) Pyrocurrent ( $I_p$ ) under two opposite poling fields. (b) Polarization curves corresponding to (a). Inset:  $I_p$  under various magnetic fields. (c)  $I_p(T)$  data under various warming rates. (d)  $I_p(T)$  curves recorded with different poling temperatures ( $T_p$  ranging from 40 to 18 K) lying above and below  $T_{E1} \sim 32$  K and  $T_C = T_{E2} \sim 25$  K. Inset: Closer view of the  $I_p(T)$  curves measured with  $T_p = 20$  and 18 K, which shows the existence of both the  $I_p$  peaks even when the poling was performed below  $T_{E1}$  and  $T_C = T_{E2}$ . For all these curves, the associated error bars are smaller than the data point markers.

higher-temperature dielectric peak at  $T_{E1}$  gets masked by the predominant presence of the  $\epsilon'$  peak at  $T_C = T_{E2}$  lying closely below  $T_{E1}$ . Despite the absence of a dielectric peak near  $T_{E1} \sim 32$  K, an emergence of a ferroelectric transition as indicated by the  $I_p$  peak at  $T_{E1} \sim 32$  K was also supported by the concurrent occurrence of the structural distortion at this temperature, as evident both from the SXR and Raman spectroscopy studies. However, the reason for the absence of a dielectric peak at  $T_{E1}$  is not fully understood in the present study. Furthermore, under various applied  $H$ , the  $I_p(T)$  curves did not show any significant change, thus suggesting the non- or minimal  $H$  dependence of  $P$ . This may be ascribed to the robustness of the spin structure of BCBO under  $H$  (as suggested by our NPD analysis). In fact, the minimal or non- $H$ -dependence of  $P$  has been reported earlier in other multiferroics [39]. As BCBO has a polar crystal structure, it may also possess a small  $P$  even at room temperature. However, such polarization, if it exists, may be very weak; thus, the resulting signal could not be detected in our room-temperature  $P$  measurements. A similar behavior was also reported in other polar multiferroics [28]. In this regard, a single-crystal study may be helpful, as polycrystalline samples often cause a large suppression in  $P$  [40]. Nevertheless, the concurrent occurrence of the lower-temperature  $I_p$  peak and FiM transition at  $T_C = T_{E2} =$

25 K indicates a close correlation between the spin and ferroelectric orders at this temperature. In general, for a magnetic system with a collinear spin order exhibiting ferroelectricity at  $T_N$  is explained via a magnetostriction mechanism [1]. By contrast, the inverse Dzyaloshinskii-Moriya interaction process is capable of explaining the ferroelectricity due to the noncollinear spin ordering, such as cycloidal or spiral phase [1]. However, as previously mentioned, the present system is already polar in the paramagnetic phase and it develops a collinear FiM spin ordering below  $T_C$ ; thus, only a slight structural alteration caused by the magnetostriction effect may further result in a change in  $P$ . In fact, our SXR study also indicated the presence of a magnetostriction effect below  $T_C$  (it will be discussed in a following section). Unlike the lower-temperature case, the higher-temperature  $I_p$  peak (at  $T_{E1} = 32$  K) occurred above the magnetic transition temperature  $T_C$ , which undoubtedly discards any possibility of a correlation between the spin and ferroelectric orders. Interestingly, our  $T$ -dependent SXR analysis and Raman spectroscopy measurements revealed a prominent structural distortion in the vicinity of  $T_{E1} = 32$  K (as will be discussed later), which might have enhanced the  $P$ , thus triggering the  $I_p$  peak. Therefore, the higher-temperature ferroelectric transition emerged independently and appeared to be solely associated with

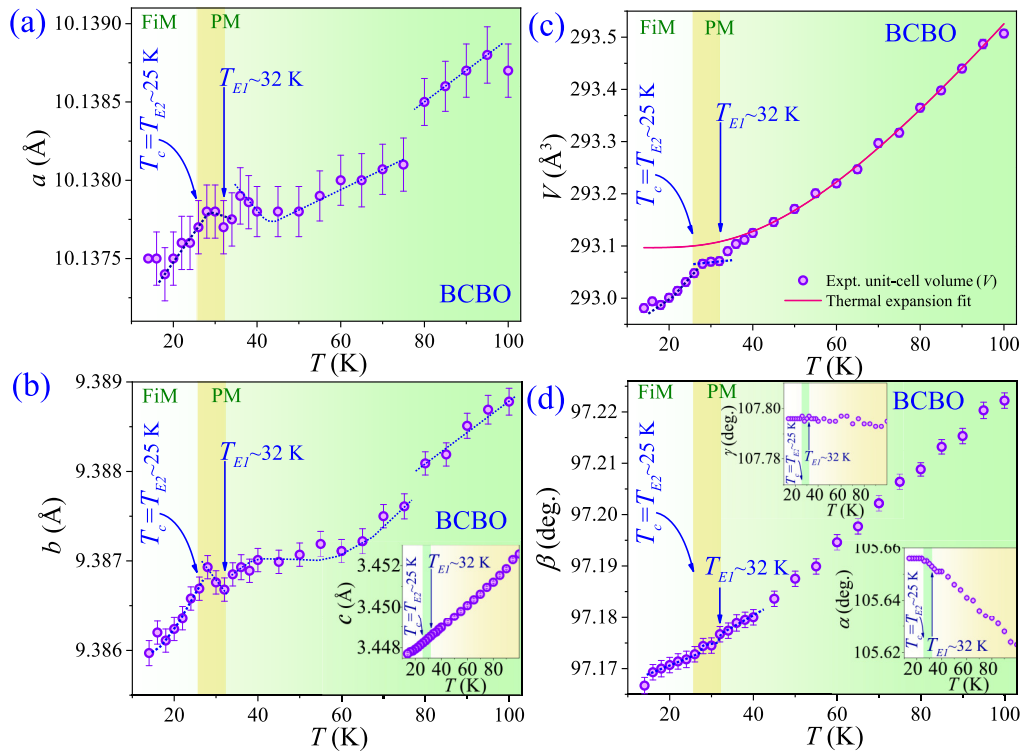


FIG. 7. (a), (b), (c), and (d), respectively, demonstrate the temperature dependence of refined lattice parameters  $a$ ,  $b$ ,  $V$ , and  $\beta$ . Blue dashed line is a guide to the eye. Inset of (b):  $T$  dependence of lattice constant  $c$ . Insets, bottom and top of (d), respectively, show  $T$  variations of lattice constants  $\alpha$  and  $\gamma$ .

the strong lattice distortion observed at  $T_{E1} = 32$  K. Thus, the present system becomes an interesting member among the NCS polar magnets showing multiferroicity. Some of such known polar magnet multiferroic systems are  $\text{Ni}_3\text{TeO}_6$ ,  $M_2\text{Mo}_3\text{O}_8$  ( $M = \text{Co}, \text{Mn}, \text{Fe}$ ), and  $R\text{FeWO}_6$  ( $R = \text{Tb}, \text{Y}, \text{Eu}, \text{Dy}, \text{Ho}$ ), which are polar in their paramagnetic phase [24–29]. Of these systems, the multiferroicity in the collinear AFM magnets, viz.,  $\text{Ni}_3\text{TeO}_6$  and  $M_2\text{Mo}_3\text{O}_8$  ( $M = \text{Co}, \text{Mn}, \text{Fe}$ ), were explained via magnetostriction mechanism. On the other hand, a spin-orbit coupling was considered to be a crucial factor in emanating the polarization change in the noncollinear magnets  $R\text{FeWO}_6$  ( $R = \text{Ho}, \text{Tb}, \text{Y}, \text{Eu}, \text{Dy}$ ) [29]. These systems exhibit multiferroicity by showing a polarization change at the onset of their magnetic ordering temperatures. Interestingly, BCBO presents a unique multiferroic property of double-ferroelectric transitions by showing polarization changes at  $T_C$  and also in the paramagnetic phase. A similar scenario of dual-ferroelectric transitions was recently reported in other multiferroic spinel Zn-ferrite system  $\text{ZnFe}_2\text{O}_4$  [37].

### E. Temperature-dependent synchrotron x-ray diffraction

High-resolution SXRDX patterns at various temperatures ranging from  $T = 100$  to 14 K were collected to gain more insight into its structural evolution, particularly in the vicinity of its magnetic and ferroelectric transition temperatures. To probe how the various Bragg peaks evolve below and above  $T_C = T_{E2}$  and  $T_{E1}$ , the SXRDX patterns at three different temperatures  $T = 18, 28$ , and 100 K are shown in Fig. S5 of the SM [30]. A few noticeable changes in the peak positions

and their intensities for various Bragg peaks can be observed, as demonstrated in Fig. S5. Since BCBO already belongs to the lowest crystal symmetry  $P1$ , a symmetry lowering is not allowed. Thus, the observed alterations in the SXRDX peaks appear to be related to the lower-temperature structural distortions, which are evident from the lattice parameter anomalies (it will be discussed in the following section).

The  $T$  variations of the refined unit-cell lattice parameters are demonstrated in Figs. 7(a)–7(d) and their insets. The  $T$  variations of lattice parameters  $a$  and  $b$  present an anomalous decrease around  $\sim 80$  K, which suggests a small structural distortion around this temperature. This appears to be a plausible reason for the observed high-temperature dielectric relaxation behavior in the vicinity of this temperature region. Our analysis suggested that this structural distortion involves significant shifts of several O atoms, thus resulting in distortion of the associated  $\text{CuO}_4$  plaquettes, which is demonstrated in Fig. S8(a) of the SM [30]. It can be further noted that the  $T$  variation of  $c$  does not exhibit any noticeable anomaly near 80 K. However, the overall changes in  $c$  (by amplitude) with varying  $T$  considerably dominates over that for both  $a$  and  $b$ . This is the reason for the apparent absence of a distinct anomaly in  $V$  near 80 K. As shown in Fig. 7(c), at least down to  $T = 40$  K, the  $V(T)$  curve reflects the typical thermal expansion behavior, which is expressed as  $V(T) = V_0[1 + \frac{A}{(e^{(\theta_D/T)} - 1)}]$ , where  $V_0$  denotes  $V$  at  $T = 0$  K,  $A$  an adjustable parameter for fitting, and  $\theta_D$  the Debye temperature. As the temperature was decreased to below 40 K, the  $V(T)$  curve showed a deviation from the thermal expansion behavior, followed by a clear slope change in the vicinity

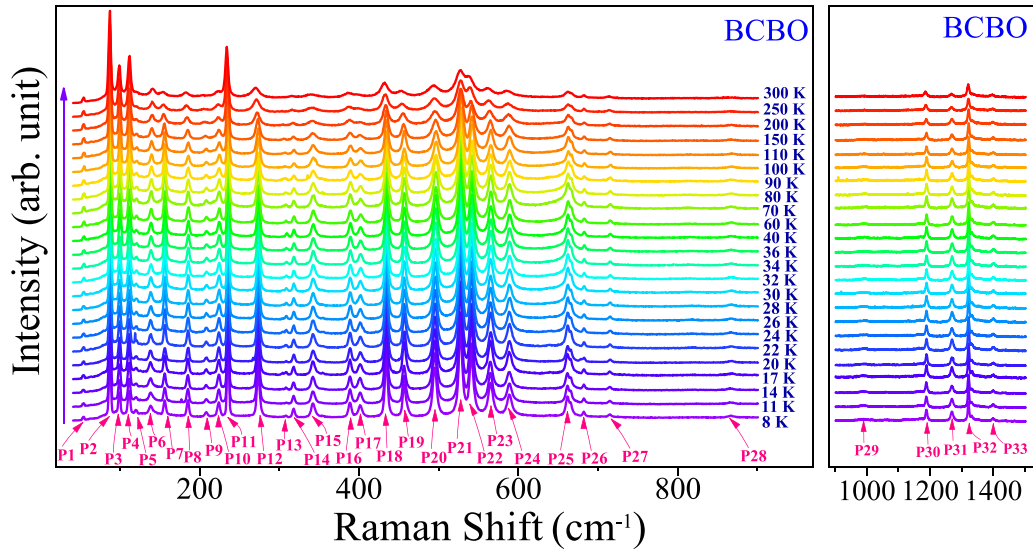


FIG. 8. Raman spectra collected at different temperatures. To increase the visibility of modes, the spectra have been demonstrated in two different segments. Left panel: Raman spectra in the range 40–900  $\text{cm}^{-1}$ . Right panel: Raman spectra in the range 900–1500  $\text{cm}^{-1}$ .

of  $T_{E1} = 32$  K. The corresponding anomalies near  $T_{E1}$  were similarly observed in the  $T$  dependence of the other lattice parameters (except for  $c$  and  $\gamma$ , where the anomalies were inconspicuous). These observations suggest the occurrence of a prominent structural distortion near  $T_{E1}$ , which may be presumably attributed for triggering the higher-temperature ( $T_{E1} \sim 32$  K) ferroelectric transition in BCBO. To get a deeper insight into this structural distortion, the thermal variations of various bond lengths and bond angles (as obtained from the SXRD data analysis) of BCBO crystal are studied, which are shown in Figs. S6 and S7 of the SM [30]. It can be observed that several of the aforementioned parameters involving various atoms of BCBO exhibited distinct anomaly near  $T_{E1}$ . This seemingly indicates that various atoms of BCBO collectively participate in the structural distortion. Since the crystal structure of BCBO is already polar in the paramagnetic phase, thus, the resulting overall structural distortion in this system appears to cause a polarization change in this polar magnetic system, which essentially gives rise to the observed  $I_p$  peak at  $T_{E1}$ . A schematic representation of the aforementioned structural distortion below  $T_{E1}$  is described in Fig. S8(b) in the SM [30]. An overall structural distortion of this system due to collective shifts of various atoms was also supported by our Raman spectroscopy study, which demonstrated a pronounced anomalous phonon softening for most of the observed Raman modes (it will be discussed in a following section).

Upon further cooling, another slope change is visible in the  $T$  variations of various lattice parameters (such as  $a$ ,  $b$ , and  $V$ ) near  $T_C \sim 25$  K (Fig. 7), which may be presumably attributed to an underlying magnetostriction effect [12]. The observed steep decrease in  $a$  and  $b$  below  $T_C$  apparently indicates that the only pairs of antiferromagnetically coupled spins Cu(1)–Cu(2) and Cu(1)–Cu(3) may be mainly responsible for this (since ferromagnetically coupled spins typically do not decrease the distance between them; instead, they increase it). On the other hand, no distinct slope change with a steep decrease was observed in the  $c(T)$  curve near  $T_C$ ,

thus showing an usual thermal expansion behavior. This is consistent with the fact that all the spins are ferromagnetically coupled along the  $c$  direction [Fig. 4(a)]. Moreover, on looking at the  $T$  dependence of various bond lengths and bond angles, as depicted in Figs. S6 and S7 in the SM [30], respectively, anomalies were clearly discerned below  $T_C = T_{E2} \sim 25$  K (in addition to the pronounced structural anomalies observed in the aforementioned parameters near  $T \sim 80$  K and  $T_{E1} \sim 32$  K). These anomalies near  $T_C = T_{E2} \sim 25$  K further indicates a magnetostriction effect owing to an emergence of various exchange interactions in the FiM ordered state. Hence, the lower-temperature  $I_p$  peak (at  $T_{E2} = T_C$ ) may have been induced by a magnetostriction effect. However, to get a better understanding of the underlying mechanism of the observed dual ferroelectricity in BCBO further studies may be required.

### F. Temperature-dependent Raman spectroscopy

A lattice distortion occurring in a system is often reflected in its phonon spectra [9,12]. Thus, to reconfirm the observed structural distortions in BCBO, we performed  $T$ -dependent Raman spectroscopy study on this system down to  $T = 8$  K, as shown in Fig. 8. No additional peaks were observed in the entire  $T$  range of study, thus precluding any global structural change, which is also consistent with the crystal symmetry  $P1$  (no. 001) of the present system (where no symmetry lowering is allowed). Based on a group theory-based symmetry analysis of BCBO structure exhibiting triclinic symmetry  $P1$  (no. 001) with a point group  $C_1$ , 75 possible modes are predicted at the  $\Gamma$  point of the Brillouin zone, which include 72 simultaneously active Raman (72A) and infrared (72A) modes, as well as three acoustic modes (3A). The phonon mode assignments of various observed Raman peaks were carried out by a phonon spectrum calculation using DFT as well as by utilizing the PHONOPY program and the Bilbao crystallographic server [41]. Details regarding the possible vibrational origins of the observed modes (designated as P1–P33 in Fig. 8) and their

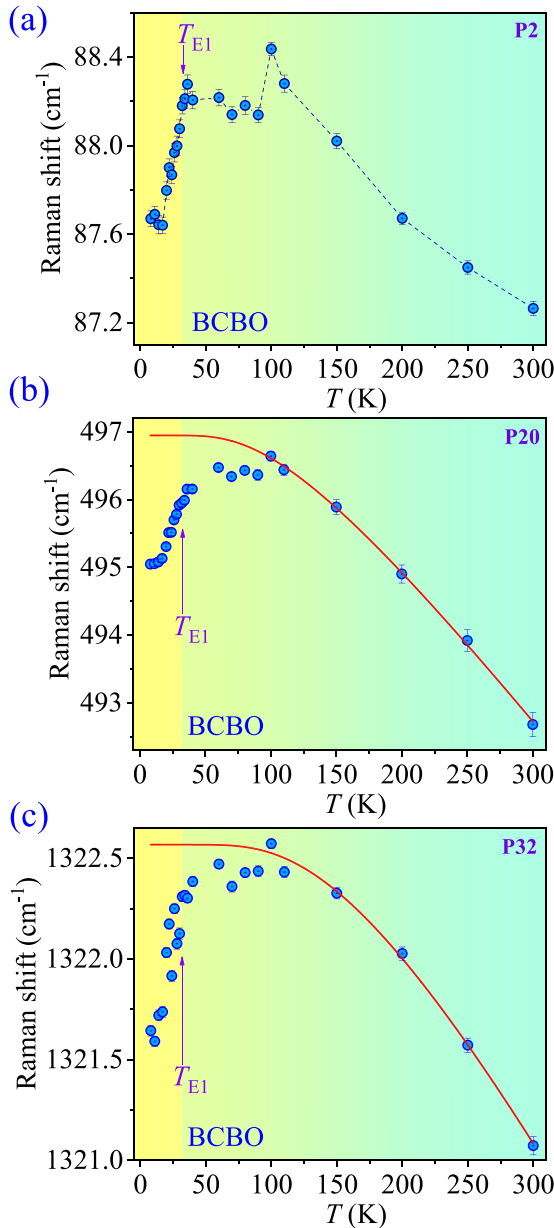


FIG. 9.  $T$  variation of phonon frequency ( $\omega$ ) for three different Raman modes (with low, intermediate, and high  $\omega$ ). Here, blue circles refer to the experimental data, whereas the red solid line represents the anharmonic fit.

symmetry assignments are summarized in Table SII of the SM [30].

To understand the thermal evolution of various Raman modes, Lorentzian peak fitting was performed on several selected Raman modes with high or moderate intensities. The obtained “phonon frequency ( $\omega$ ) variation as a function of  $T$ ” for only three different Raman modes from three different  $\omega$  ranges (i.e., with low, intermediate, and high  $\omega$ ) are shown in Fig. 9, whereas such curves for all the analyzed modes are shown in Fig. S9 of the SM to avoid complexity [30]. Generally, in the absence of spin-phonon or electron-phonon coupling or structural change,  $\omega(T)$  describes an anharmonic behavior, which is expressed as  $\omega_{\text{anh}}(T) =$

$\omega_0 - C(1 + 2/\frac{\hbar\omega_0}{e^{k_B T} - 1})$ , where  $\omega_0$  and  $C$  denote adjustable parameters,  $k_B$  the Boltzmann constant, and  $\hbar$  the reduced Planck constant [10,12,42,43]. According to this relation, the  $\omega(T)$  curve of a Raman mode is expected to increase (hardening) gradually as  $T$  decreases, followed by a plateau at lower  $T$ . In the present study, all the modes exhibited a monotonic increase in  $\omega$  as  $T$  decreased at least down to  $T = 100$  K (Figs. 9 and S8). Hence, most of the modes primarily reflected the anharmonic behavior down to  $T = 100$  K. For modes P2, P3, P4, and P11, although the  $\omega(T)$  curves could not be fitted satisfactorily using the anharmonic law even in the high- $T$  region, they clearly demonstrated an increasing  $\omega$  as  $T$  decreased, which in turn supports the anharmonic behavior. Interestingly, for all modes, a dramatic drop or a clear downturn deviation (i.e., anomalous phonon softening) from the anharmonic curve near  $T = 80$  K was shown in the  $\omega(T)$  curves. As  $T = 80$  K lies much above the  $T_C = 25$  K of BCBO, the role of spin-phonon coupling can be precluded for this case. Meanwhile, the highly insulating nature of BCBO rules out the role of electron-phonon coupling in the observed phonon softening. Nevertheless, our SXRD results indicated structural distortion near 80 K, which triggered dielectric relaxation near this region. Hence, the origin of the observed anomalous phonon softening near  $T = 80$  K may be attributed to the structural distortion at this temperature.

Upon further lowering the temperature, another pronounced anomaly was observed in the  $\omega(T)$  curves, which appeared in the form of a sharp anomalous phonon softening near  $T_{E1} \sim 32$  K for all the Raman modes studied, as evident from Figs. 9 and S8 [30]. A similar anomalous phonon softening or hardening at the onset of magnetic ordering is also observed in systems exhibiting spin-phonon coupling [12,44,45]. For the present case, the anomalous phonon softening commences in the paramagnetic phase near  $T_{E1}$ , where a pronounced structural distortion takes place (as suggested by the SXRD study). Moreover, no trace of a short-range magnetic ordering above  $T_C = 25$  K was detected in our magnetization or NPD measurements for BCBO. Thus, the observed anomalous phonon softening near  $T_{E1}$  essentially validates the presence of a strong structural distortion at this temperature, which appears to trigger the ferroelectric transition at that temperature. In fact, as  $T_C$  and  $T_{E1}$  are close to each other, the role of a possible spin-phonon coupling in the observed anomalous phonon softening may also be considered (below  $T_C$ ). However, the signal of the spin-phonon coupling, if it exists, gets substantially suppressed due to the sharp anomalous phonon softening at  $T_{E1}$  due to the strong structural distortion.

In addition, the  $T$  dependence of full width at half maximum or linewidth ( $\Gamma$ ) curves for various Raman modes are demonstrated in Fig. S10 of the SM [30]. Generally, a  $\Gamma(T)$  curve of a Raman mode (related to the phonon lifetime) following the anharmonic law describes a decreasing behaviour with lowering temperature and thus plateauing at lower temperatures. For the present case, sizable anomalies in the form of anomalous broadening can be observed in  $\Gamma(T)$  curves near  $T = 80$  K as well as  $T_{E1} = 32$  K, for various Raman modes (Fig. S10). Thus, the observation of the simultaneously occurring anomalies in both  $\omega(T)$  and  $\Gamma(T)$  curves essentially attest to the structural distortions occurring near the aforementioned

temperature regions, thus corroborating the SXR D results. Nevertheless, our present study reveals an interesting multiferroic system exhibiting simultaneous FiM and ferroelectric transitions at  $T_C = T_{E1} = 25$  K and another solely structural distortion-driven ferroelectric transition at  $T_{E1} \sim 32$  K. This eventually places the present system among the very unique and rare materials. Further single-crystal study and detailed theoretical calculations on BCBO may facilitate in providing deeper insight into the phenomena observed in this system.

#### IV. CONCLUSIONS

A comprehensive study performed on a layered noncentrosymmetric spin-1/2 ferrimagnetic system,  $\text{Bi}_2\text{Cu}_5\text{B}_4\text{O}_{14}$ , revealed its unconventional multiferroic property, which demonstrated a strongly coupled behavior of various microscopic degrees of freedom, i.e., spins, lattices, dipoles, and phonons. A very stable long-range ferrimagnetic ( $\uparrow\downarrow\downarrow\downarrow$ ) order that remained unchanged, even under a high magnetic field of  $H = 10$  T, was observed at  $T_C = 25$  K. A dielectric

peak showing a clear magnetodielectric effect, which is accompanied by a magnetostriction effect-driven ferroelectric transition emerged concomitantly with a ferrimagnetic ordering at  $T_C = T_{E2} = 25$  K. Interestingly, another ferroelectric transition commenced in the paramagnetic region at  $T_{E1} = 32$  K, which is purely associated with a strong structural distortion in the system, as evidenced by the results of SXR D analysis. Moreover, the observation of prominent anomalous phonon softening in the Raman spectra at  $T_{E1} = 32$  K further supported the structural distortion at that temperature, which appeared to have played the pivotal role in the emanation of ferroelectric polarization at that temperature.

#### ACKNOWLEDGMENTS

This work was supported by the Ministry of Science and Technology (presently known as the National Science and Technology Council), Taiwan, under Grants No. MOST 111-2811-M-110-012, No. MOST 111-2923-M-110-001, and No. MOST 111-2112-M-110-017.

- 
- [1] D. Khomskii, Classifying multiferroics: Mechanisms and effects, *Physics (College Park, MD)* **2**, 20 (2009).
- [2] T. Kimura, Spiral magnets as magnetoelectrics, *Annu. Rev. Mater. Res.* **37**, 387 (2007).
- [3] M. Fiebig, Revival of the magnetoelectric effect, *J. Phys. D: Appl. Phys.* **38**, R123 (2005).
- [4] W. Eerenstein, N. D. Mathur, and J. F. Scott, Multiferroic and magnetoelectric materials, *Nature (London)* **442**, 759 (2006).
- [5] S. W. Cheong and M. Mostovoy, Multiferroics: A magnetic twist for ferroelectricity, *Nat. Mater.* **6**, 13 (2007).
- [6] L. Zhou, J. Dai, Y. Chai, H. Zhang, S. Dong, H. Cao, S. Calder, Y. Yin, X. Wang, X. Shen, Z. Liu, T. Saito, Y. Shimakawa, H. Hojo, Y. Ikuhara, M. Azuma, Z. Hu, Y. Sun, C. Jin, and Y. Long, Realization of large electric polarization and strong magnetoelectric coupling in  $\text{BiMn}_3\text{Cr}_4\text{O}_{12}$ , *Adv. Mater.* **29**, 1703435 (2017).
- [7] N. A. Spaldin and R. Ramesh, Advances in magnetoelectric multiferroics, *Nat. Mater.* **18**, 203 (2019).
- [8] M. Mostovoy, Ferroelectricity in Spiral Magnets, *Phys. Rev. Lett.* **96**, 067601 (2006).
- [9] B. Poojitha, A. Rathore, A. Kumar, and S. Saha, Signatures of magnetostriction and spin-phonon coupling in magnetoelectric hexagonal  $15\text{-RBaMnO}_3$ , *Phys. Rev. B* **102**, 134436 (2020).
- [10] A. Pal, T. W. Kuo, C. H. Hsu, D. C. Kakarla, A. Tiwari, M. C. Chou, A. Patra, P. Yanda, E. Blundo, A. Polimeni, A. Sundaresan, F. C. Chuang, and H. D. Yang, Interplay of lattice, spin, and dipolar properties in  $\text{CoTeMoO}_6$ : Emergence of Griffiths-like phase, metamagnetic transition, and magnetodielectric effect, *Phys. Rev. B* **105**, 024420 (2022).
- [11] M. Fiebig, T. Lottermoser, D. Meier, and M. Trassin, The evolution of multiferroics, *Nat. Rev. Mater.* **1**, 16046 (2016).
- [12] A. Pal, C. H. Huang, T. W. Yen, P. H. Lee, Y. H. Chang, C. H. Yeh, T. W. Kuo, A. Tiwari, D. C. Kakarla, S. M. Huang, M. C. Chou, H. S. Kunwar, S. Rana, V. G. Sathe, B. H. Chen, Y. C. Chuang, and H. D. Yang, Spin-induced strongly correlated magnetodielectricity, magnetostriction effect, and spin-phonon coupling in helical magnet  $\text{Fe}_3(\text{PO}_4)\text{O}_3$ , *Phys. Rev. B* **106**, 094404 (2022).
- [13] U. Adem, L. Wang, D. Fausti, W. Schottenhamel, P. H. M. vanLoosdrecht, A. Vasiliev, L. N. Bezmaternykh, B. Büchner, C. Hess, and R. Klingeler, Magnetodielectric and magnetoelectric coupling in  $\text{TbFe}_3(\text{BO}_3)_4$ , *Phys. Rev. B* **82**, 064406 (2010).
- [14] K. Kimura, P. Babkevich, M. Sera, M. Toyoda, K. Yamauchi, G. S. Tucker, J. Martius, T. Fennell, P. Manuel, D. D. Khalyavin, R. D. Johnson, T. Nakano, Y. Nozue, H. M. Rønnow, and T. Kimura, Magnetodielectric detection of magnetic quadrupole order in  $\text{Ba}(\text{TiO})\text{Cu}_4(\text{PO}_4)_4$  with  $\text{Cu}_4\text{O}_{12}$  square cupolas, *Nat. Commun.* **7**, 13039 (2016).
- [15] J. W. Kim, S. Khim, S. H. Chun, Y. Jo, L. Balicas, H. T. Yi, S. W. Cheong, N. Harrison, C. D. Batista, J. Hoon Han, and K. Hoon Kim, Manifestation of magnetic quantum fluctuations in the dielectric properties of a multiferroic, *Nat. Commun.* **5**, 4419 (2014).
- [16] G. A. Petrakovskii, K. A. Sablina, A. I. Pankrats, D. A. Velikanov, A. D. Balaev, O. A. Bayukov, V. I. Tugarinov, A. M. Vorotynov, A. D. Vasil'ev, G. V. Romanenko, and Y. G. Shvedenkov, Synthesis of the new oxocuprate  $\text{Bi}_2\text{Cu}_5\text{B}_4\text{O}_{14}$  and investigation of its structural, magnetic, and resonant properties, *Phys. Solid State* **44**, 1339 (2002).
- [17] S. Pan, J. P. Smit, M. R. Marvel, E. S. Stampler, J. M. Haag, J. Baek, P. S. Halasyamani, and K. R. Poeppelmeier, Synthesis, crystal structure, and nonlinear optical properties of  $\text{Bi}_2\text{Cu}_5\text{B}_4\text{O}_{14}$ , *J. Solid State Chem.* **181**, 2087 (2008).
- [18] U. Arjun, V. Ramakrishnan, and R. Nath, Structural and magnetic properties of spin-1/2 layered ferrimagnet  $\text{Bi}_2\text{Cu}_5\text{B}_4\text{O}_{14}$ , *J. Alloys Compd.* **683**, 205 (2016).
- [19] L. Balents, Spin liquids in frustrated magnets, *Nature (London)* **464**, 199 (2010).
- [20] D. LeBoeuf, N. Doiron-Leyraud, J. Levallois, R. Daou, J. B. Bonnemaison, N. E. Hussey, L. Balicas, B. J. Ramshaw, R. Liang, S. Adachi, C. Proust, and L. Taillefer, Electron

- pockets in the Fermi surface of hole-doped high- $T_c$  superconductors, *Nature (London)* **450**, 533 (2007).
- [21] T. Kimura, Y. Sekio, H. Nakamura, T. Siegrist, and A. P. Ramirez, Cupric oxide as an induced-multiferroic with high- $T_C$ , *Nat. Mater.* **7**, 291 (2008).
- [22] L. Zhao, M. T. Fernández-Díaz, L. H. Tjeng, and A. C. Komarek, Oxyhalides: A new class of high- $T_C$  multiferroic materials, *Sci. Adv.* **2**, 1600353 (2016).
- [23] S. Seki, X. Z. Yu, S. Ishiwata, and Y. Tokura, Observation of skyrmions in a multiferroic material, *Science* **336**, 198 (2012).
- [24] Y. S. Tang, S. M. Wang, L. Lin, C. Li, S. H. Zheng, C. F. Li, J. H. Zhang, Z. B. Yan, X. P. Jiang, and J. M. Liu, Collinear magnetic structure and multiferroicity in the polar magnet  $\text{Co}_2\text{Mo}_3\text{O}_8$ , *Phys. Rev. B* **100**, 134112 (2019).
- [25] Y. Wang, G. L. Pascut, B. Gao, T. A. Tyson, K. Haule, V. Kiryukhin, and S. W. Cheong, Unveiling hidden ferrimagnetism and giant magnetoelectricity in polar magnet  $\text{Fe}_2\text{Mo}_3\text{O}_8$ , *Sci. Rep.* **5**, 12268 (2015).
- [26] T. Kurumaji, S. Ishiwata, and Y. Tokura, Diagonal magnetoelectric susceptibility and effect of Fe doping in the polar ferrimagnet  $\text{Mn}_2\text{Mo}_3\text{O}_8$ , *Phys. Rev. B* **95**, 045142 (2017).
- [27] Y. S. Oh, S. Artyukhin, J. J. Yang, V. Zapf, J. W. Kim, D. Vanderbilt, and S. W. Cheong, Non-hysteretic colossal magnetoelectricity in a collinear antiferromagnet, *Nat. Commun.* **5**, 3201 (2014).
- [28] S. Ghara, E. Suard, F. Fauth, T. T. Tran, P. S. Halasyamani, A. Iyo, J. Rodríguez-Carvajal, and A. Sundaresan, Ordered aeschynite-type polar magnets  $\text{RFeWO}_6$  ( $R = \text{Dy}, \text{Eu}, \text{Tb}$ , and  $\text{Y}$ ): A new family of Type-II multiferroics, *Phys. Rev. B* **95**, 224416 (2017).
- [29] M. Adnani, M. Gooch, L. Deng, S. Agrestini, J. Herrero-Martin, H.-C. Wu, C.-K. Chang, T. Salavati-fard, N. Poudel, J. L. García-Muñoz, S. Daneshmandi, Z. Wu, L. C. Grabow, Y.-C. Lai, H.-D. Yang, E. Pellegrin, and C.-W. Chu, Magnetocapacitance effect and magnetoelectric coupling in Type-II multiferroic  $\text{HoFeWO}_6$ , *Phys. Rev. B* **103**, 094110 (2021).
- [30] See Supplemental Material at <http://link.aps.org/supplemental/10.1103/PhysRevB.107.184430> for the additional details of SXRD, computational and experimental methods, neutron diffraction analysis, and Raman spectroscopy.
- [31] A. J. Studer, M. E. Hagen, and T. J. Noakes, Wombat: The high-intensity powder diffractometer at the OPAL reactor, *Phys. B Condens. Matter* **385-386**, 1013 (2006).
- [32] H. Takatsu, H. Yoshizawa, S. Yonezawa, and Y. Maeno, Critical behavior of the metallic triangular-lattice heisenberg antiferromagnet  $\text{NiTe}_2\text{O}_5$ , *Phys. Rev. B* **79**, 104424 (2009).
- [33] P. K. Yadav, M. Tolkiehn, and C. Upadhyay, Dielectric relaxations in  $\text{Ho}_2\text{Ti}_2\text{O}_7$  and  $\text{Dy}_2\text{Ti}_2\text{O}_7$  pyrochlores, *J. Phys. Chem. Solids* **134**, 201 (2019).
- [34] D. C. Kakarla, Z. H. Yang, H. C. Wu, T. W. Kuo, A. Tiwari, W.-H. Li, C. H. Lee, Y.-Y. Wang, J.-Y. Lin, C. K. Chang, B. H. Chen, C. W. Wang, C. A. Lee, M. M. C. Chou, and H. D. Yang, Single crystal growth and structural, magnetic, and magnetoelectric properties in spin-frustrated bow-tie lattice of  $\alpha\text{-Cu}_5\text{O}_2(\text{SeO}_3)_2\text{Cl}_2$ , *Mater. Adv.* **2**, 7939 (2021).
- [35] A. Tiwari, D. C. Kakarla, G. Macam, C. H. Hsu, F. C. Chuang, H. C. Wu, T. W. Kuo, A. Pal, H. Chou, D. P. Gulo, H. L. Liu, Y. C. Chuang, Y. C. Lai, C. A. Lee, M. M. C. Chou, and H. D. Yang, Spin-lattice-charge coupling in quasi-one-dimensional spin-chain  $\text{NiTe}_2\text{O}_5$ , *Phys. Rev. Mater.* **6**, 044409 (2022).
- [36] M. Liu, L. Lin, Y. Zhang, S. Li, Q. Huang, V. O. Garlea, T. Zou, Y. Xie, Y. Wang, C. Lu, L. Yang, Z. Yan, X. Wang, S. Dong, and J.-M. Liu, Cycloidal magnetism driven ferroelectricity in double tungstate  $\text{LiFe}(\text{WO}_4)_2$ , *Phys. Rev. B* **95**, 195134 (2017).
- [37] J. K. Dey, A. Chatterjee, A. C. Dippel, O. Gutowski, M. v. Zimmermann, S. Majumdar, and S. Giri, Rhombohedral distortion-driven ferroelectric order and exchange bias effect in geometrically frustrated  $\text{ZnFe}_2\text{O}_4$ , *Phys. Rev. Mater.* **5**, 014410 (2021).
- [38] S. Mukherjee, G. Manna, P. Saha, S. Majumdar, and S. Giri, Ferroelectric order with a linear high-field magnetoelectric coupling in  $\text{Na}_2\text{Co}_2\text{TeO}_6$ : A proposed Kitaev compound, *Phys. Rev. Mater.* **6**, 054407 (2022).
- [39] F. Wang, T. Zou, Y. Liu, L. Q. Yan, and Y. Sun, Persistent multiferroicity without magnetoelectric effects in  $\text{CuO}$ , *J. Appl. Phys.* **110**, 054106 (2011).
- [40] L. Zhao, C.-H. Du, and A. C. Komarek, Spin-driven pyroelectricity in  $\text{Ni}_3\text{TeO}_6$  without ferroelectric signatures of the transition at Néel temperature, *Phys. Status Solidi - Rapid Res. Lett.* **11**, 1700073 (2017).
- [41] E. Kroumova, M. I. Aroyo, J. M. Perez-Mato, A. Kirov, C. Capillas, S. Ivantchev, and H. Wondratschek, Bilbao crystallographic server: Useful databases and tools for phase-transition studies, *Phase Transitions* **76**, 155 (2003).
- [42] M. Balkanski, R. F. Wallis, and E. Haro, Anharmonic effects in light scattering due to optical phonons in silicon, *Phys. Rev. B* **28**, 1928 (1983).
- [43] A. Pal, K. Anand, N. Patel, A. Das, S. Ghosh, P. T.-W. Yen, S.-M. Huang, R. K. Singh, H. D. Yang, A. K. Ghosh, and S. Chatterjee, Interplay of spin, phonon, and lattice degrees in a hole-doped double perovskite: Observation of spin-phonon coupling and magnetostriction effect, *J. Appl. Phys.* **132**, 223906 (2022).
- [44] E. Granado, A. García, J. A. Sanjurjo, C. Rettori, I. Torriani, F. Prado, R. D. Sánchez, A. Caneiro, and S. B. Oseroff, Magnetic ordering effects in the Raman spectra of  $\text{La}_{1-x}\text{Mn}_{1-x}\text{O}_3$ , *Phys. Rev. B* **60**, 11879 (1999).
- [45] A. Pal, K. Anand, T. W. Yen, A. Patra, A. Das, S. M. Huang, E. Blundo, A. Polimeni, H. D. Yang, and S. Chatterjee, Magnetic properties and coupled spin-phonon behavior in quasi-one-dimensional screw-chain compound  $\text{BaMn}_2\text{V}_2\text{O}_8$ , *Phys. Rev. Mater.* **7**, 014402 (2023).